ECS Transactions, 61 (27) 155-163 (2014)
10.1149/06127.0155ecst ©The Electrochemical Society

Nanostructured Electrodes via Electrostatic Spray Deposition for Energy Storage System

C. Chen[a], R. Agrawal[a], T. K. Kim[a], X. Li[b], W. Chen[c], Y. Yan[d], M. Beidaghi[e], V. Penmatsa[a] and C. Wang[a]

[a] Department of Mechanical and Materials Engineering, Florida International University, Miami, Florida 33174, USA
[b] Department of Mechanical and Materials Engineering, University of Western Ontario, ON, Canada
[c] Advanced Membranes and Porous Materials Center at King Abdullah University of Science and Technology, Thuwal, Saudi Arabia
[d] Max-Planck Institute for Solid State Research, Stuttgart, Germany
[e] Department of Mechanical Engineering and Mechanics Drexel University, Philadelphia, PA 19104, USA

Energy storage systems such as Li-ion batteries and supercapacitors are extremely important in today's society, and have been widely used as the energy and power sources for portable electronics, electrical vehicles and hybrid electrical vehicles. A lot of research has focused on improving their performance; however, many crucial challenges need to be addressed to obtain high performance electrode materials for further applications. Recently, the electrostatic spray deposition (ESD) technique has attracted great interest to satisfy the goals. Due to its many advantages, the ESD technique shows promising prospects compared to other conventional deposition techniques. In this paper, our recent research outcomes related to the ESD derived anodes for Li-ion batteries and other applications is summarized and discussed.

1. Introduction

With the rapid development of modern society and global economy, the demand for electrical energy has greatly increased. To fulfill the urgent demands, considerable research effort has been focused on designing and developing energy conversion and storage devices with high performance. Among many candidates, lithium ion batteries (LIBs) have been considered as promising energy storage devices for many applications, especially for electric vehicles (EVs), hybrid electric vehicles (HEVs) and portable electronics [1-5].

A typical LIB consists of a cathode (such as $LiCoO_2$, $LiMn_2O_4$ etc.), an anode (such as graphite, Si, SnO_2 etc.), a separator (such as: porous polypropylene membrane) and an electrolyte ($LiPF_6$ in organic solvent mixture). During the charge-discharge process, lithium ions reversibly move between the cathode and anode. The total capacity of LIB is decided by both anode and cathode capacities. Although developing new cathode

materials with much higher energy capacities than conventional cathode materials is one of the biggest challenges, the total capacity will also benefit from increased energy capacities from anode materials. For the commercial LIB, graphite is usually selected as the anode material, which has a theoretical capacity of 372 mAh/g based on LiC_6 structure [6-7]. Though metallic lithium has higher specific capacity (3862 mAh/g), the formation of dendrites on lithium due to non-uniform current distribution can lead to internal shorting and cause the battery to fail [8]. Therefore, intensive research has been focused on improving the performance of anode materials with higher energy capacities.

Based on different reaction mechanisms, anode materials are classified into three categories: (1) intercalation-de-intercalation; (2) alloying-de-alloying; (3) conversion reaction. Graphite is a good example of the first category, in which lithium ions intercalate and de-intercalate into the anode structure without destroying it during cycling. The major drawback for these materials is the limited available intercalation sites for lithium ions which results in low theoretical capacities [6-7]. The second category of anode materials comprises materials such as Si [9], Sn [10] and SnO_2 [11], etc. Alloying reaction will occur between lithium ions and active materials during discharge and the resulting alloy will decompose and release lithium ions during the charge process. Alloying based anode materials usually possess high theoretical capacities but during cycling, the huge volume change results in the electrode failure by cracking, crumbling, pulverization and loss of active materials. Conversion reaction usually takes place in transition metal oxides, nitrides, phosphides and sulfides. In discharge process, the transition-metal compound will be reduced to transition metal particles and dispersed in Li_2O matrix. The low electrical conductivity of transition metal compounds together with the volume change and aggregation of transition metal particles limit the performance of these materials [12-15].

Progress in LIB technology has benefited greatly by moving from conventional to nanostructured electrodes [16]. The use of nano-structured materials significantly (1) enhances the efficiency in utilizing the electrode material; (2) enhances the rate capability because of the reduced diffusion path way and (3) reduces the strain and stress during charge and discharge. The electrostatic spray deposition (ESD) technique, developed by Schoonman and coworkers, is a versatile process that can be used to prepare different films with various morphologies at nano-scale, such as dense, porous, cross-linked, and sponge-like structures [17]. Recently, we have focused on developing binder free thin film anode materials with various structures. In this paper, our previous efforts and most recent results is summarized and presented.

2. Electrostatic spray deposition (ESD) technique

Figure 1 shows the experimental set-up for the ESD technique. A syringe is used to supply the precursor to the needle. High DC voltage is applied between the needle and the substrate, which can be heated to a desired temperature. The detailed ESD process has been studied and discussed in other works [18-21]. In brief, the precursor solution is atomized into the aerosol by high electric field and is attracted to the heated substrate by electric field. Solvent evaporation and chemical reactions occur during the spray and landing of the drops. By changing the experimental parameters, such as precursor, concentration, flow rate, voltage, temperature, substrate etc., the structures and morphologies can be designed and controlled.

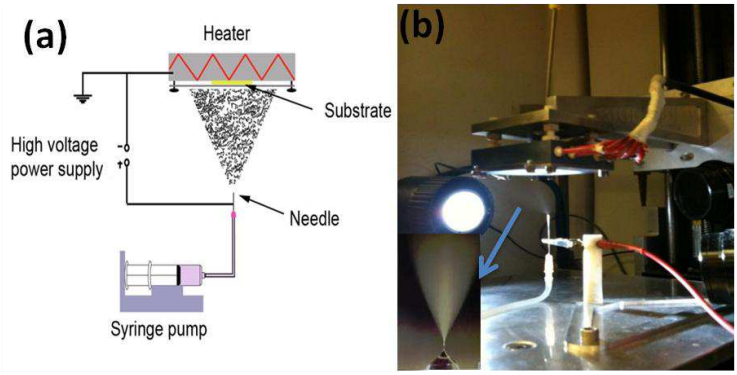

Figure 1. (a) Schematic drawing and (b) practical image of the ESD experimental set-up.

3. Application of electrostatic spray deposition

Our research based on ESD has covered several aspects: LIBs, micro-batteries, micro-supercapacitors and micro-sensors. Here we will mainly focus on electrode materials for LIBs and give brief summary for other applications.

3.1 Porous Core-Shell Sn@Carbon Composite Anode

Intensive research efforts have focused on looking for alternative anode materials with higher discharge capacities, such as Si, Sn, and Ge. Due to its high theoretical specific capacity of about 994 mAh/g, corresponding to $Li_{4.4}Sn$, Sn has been one of the most promising candidates for future LIBs. However, during the alloying process, a maximum of 4.4 lithium ions react with Sn to form $Li_{4.4}Sn$ alloy, and such reaction induces a large volume change of 259%. Electrode failure is the major problem caused by the large volume change and leads to a poor cycle performance. In order to better address this challenge, several approaches have been used such as, porous Sn, nanoscaled Sn, Sn composites (with inactive/active matrix), and Sn based alloys. The mechanical stress has been relieved to some extent by the pore or matrix components.

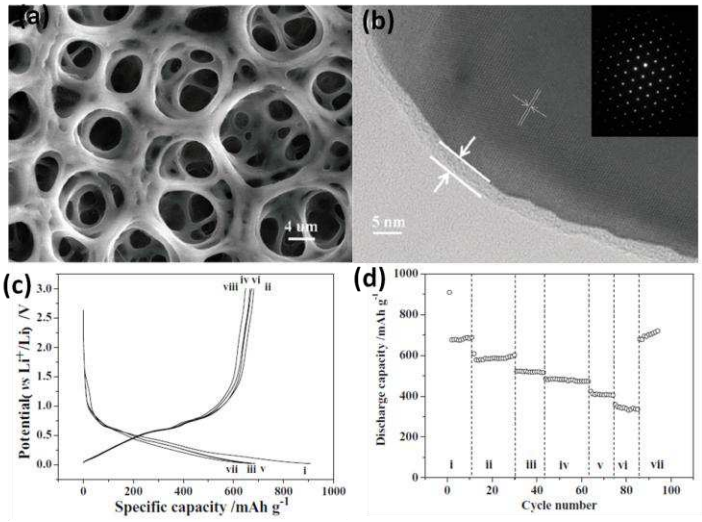

Figure 2. (a) SEM and (b) HRTEM images, (c) charge/discharge curves at the current density of 25 mA/g and (d) Rate capability at: (i) 25, (ii) 100, (iii) 150, (iv) 200, (v) 250, (vi) 300, (vii) 25 mA/g of Sn@carbon composite after heat treatment at 900 ^{0}C.

Recently we synthesized porous Sn@carbon composites on nickel foam substrate through ESD followed by a heat-treatment [10]. The resulting porous structure is shown in Figure 2 (a) and the thin carbon coating (~2.3 nm) on Sn structure is confirmed by (b) high resolution transmission electron microscope (HRTEM). The charge/discharge profile in Figure 3 (c) is typical for Sn based anode and gives an initial columbic efficiency of 74.1%, corresponding to 907 mAh/g and 672 mAh/g for initial discharge and charge capacities, respectively. For the rate capability, as shown in Figure 3 (d), the discharge capacity decreases as the current densities increases. This is because of the low diffusion rate of the lithium ions into anodes at higher rates. However, a steady discharge capacity is maintained at every current density. When charged back in low current density, the capacities reaches the same and even slightly higher capacities in group i at the same rate. This validates the structural stability of the composite which is also confirmed by the SEM images of disassembled cell after 315 cycles. It is demonstrated that Sn@carbon composite fabricated by ESD improved the lithium ion battery performance. Besides Sn based materials, other alloying reaction materials, such as SnO_2 based materials have also been studied in our group [22-23] and different levels of enhancement were achieved.

3.2 Hierarchically Macro-Mesoporous Sponge-like Fe_2O_3 Anode

Since the release of the first paper of using transition-metal oxides as anode materials for LIBs in 2000 by Tarascon [24], much research has been carried out based on this type of materials. Although they usually have higher theoretical capacities than traditional anode materials such as graphite, several drawbacks limit their performance. To further improve the performance, 3D inter-connected nanostructures have been proposed due to the high surface area and good ionic conductivity. ESD is a good choice to fabricate such structures. For example, carbon-free porous nickel foam supported-hierarchical macro-mesoporous Fe_2O_3 (HP-Fe_2O_3) thin film electrodes fabricated by ESD show promising electrochemical performance. Porous Fe_2O_3 films and the porous nickel foam current collector could offer enough space to buffer the volume change during charge/discharge and also can be beneficial for better contractions between the electrolyte and active materials. This improves both the electronic and ionic conductivity during charge/discharge processes. An improved rate capability and good capacity retention at high rates were also observed.

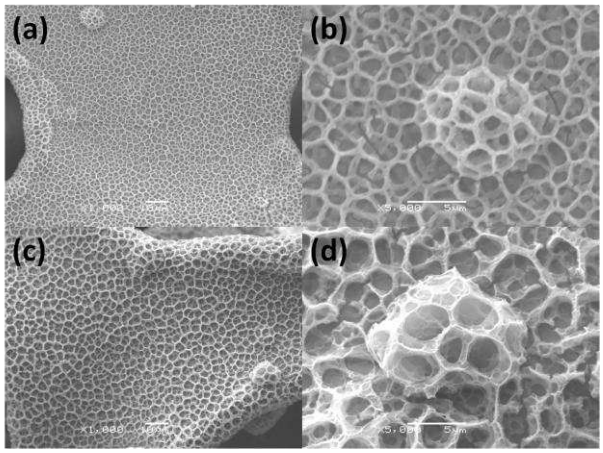

Figure 3. SEM images of electrodes derived from solution 1 (a-b) and 2 (c-d).

Since the solvents used in the precursor solution may have an influence on the microstructures and electrochemical performance of the deposited film [25], two different systems of solvents were studied: (1) ethanol: glycol: butyle carbitol (4:1:1); (2) pure 1.2-propanediol. However, the resulting microstructures did not exhibit much identical differences between two samples, as shown in figure 3. The as-deposited thin films display a hierarchically porous structure with a fully interconnected macro and meso-porous network. The distribution of macropores' diameters ranges from 100 nm to 4 μm presumably resulting from the gradual evaporation and decomposition of organic solvents. The magnified image (Figure 3 b and d) reveal in detail that these macroporous walls consisted of cross-linked mesopores. Such porous networks are expected to offer a continuous electronic pathway as well as good stress buffer area during the cycling.

Both Fe_2O_3 thin films derived from solution 1 and solution 2 were tested for their electrochemical performance versus Li^+ under galvanostatic conditions between a voltage window of 0.01–3.0 V (vs. Li^+). Figure 4 (a) and (c) show the CV curves at the 1st, 2nd, 3rd and 10th cycles and (b) and (d) show the cycle voltage versus capacity profiles for the first three cycles of both electrodes. Two electrodes display similar CV curves and are consistent with other reported amorphous Fe_2O_3 electrodes [26]. In charge-discharge curve of solution 1 electrode, it shows a long voltage plateau at about 1 V followed by a sloping discharge curve down to a cut-off voltage of 0.01V during the first discharge step. This long slope corresponds to the full reduction of Fe_2O_3 into Fe^0/Li_2O. The first discharge step delivers a specific capacity of 2554 mAh/g, which is significantly higher than the theoretical capacity of Fe_2O_3. This extra capacity is attributed to the formation of the irreversible solid electrolyte interface (SEI) film. The formation of this layer is associated with the decomposition of the electrolyte and the formation of Li^+ organic compounds. After the first discharge, the 1 V discharge plateau disappears, indicating a heterogeneous reaction mechanism of lithium insertion and extraction. The first charge process gives a capacity of 1245 mAh/g which leads to a low columbic efficiency of 51.2% for the first cycle. For the second and third cycles, most of the discharge capacities were maintained. Compared to the electrode from solution 1, the electrode from solution 2 delivered 2366 mAh/g discharge capacity for the first cycle and a columbic efficiency of 46.4%.

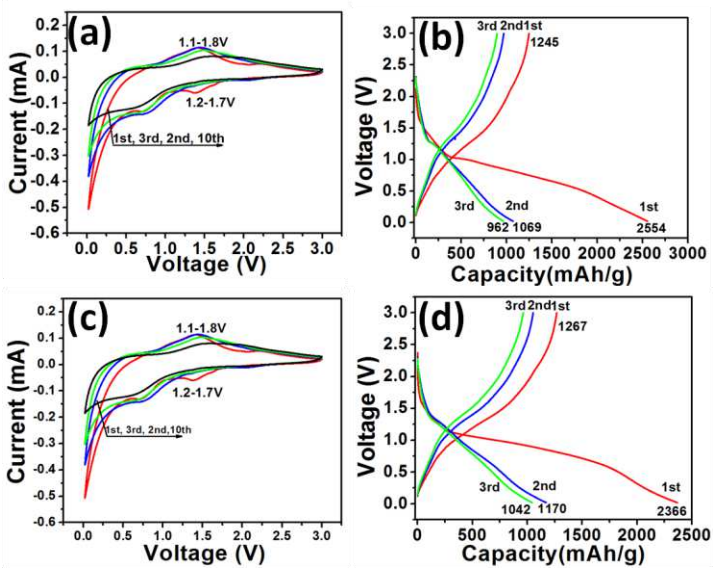

Figure 4. CV and charge-discharge curves for the electrodes derived from solution 1 (a) and (b); and solution 2 (c) and (d).

Figure 5 (a) shows the long term cyclability of both samples. Capacity of electrode from solution 1 stabilized after first ten cycles and a slight capacity increase was observed starting from the 70th cycle. For electrode from sample 2, the capacity stabilization started from around the 20th cycle. At the 100th cycle, a higher capacity of 885 mAh/g capacity was obtained from solution 1 electrode compare to 663 mAh/g capacity from solution 2 electrode. Rate capability tests were also performed after the cyclability test, as shown in figure 5 (b). The capacity decreased from 885 to 455 mAh/g and 663 to 291 mAh/g for solution 1 electrode and solution 2 electrode, respectively, when the C rate increased from 0.5 C to 20 C. The outstanding reversible capacity, capacity retention and rate capability of both electrodes are undoubtedly due to their special porous morphology. As noticed in figure 5, the electrode from solution 1 performed even better than that from solution 2. As mentioned in the previous discussion that both electrodes have similar SEM images, CV and charge-discharge profile, further study is required to find out the cause of the varied performance. There is another interesting phenomena that after the 20 C test, both electrodes show increased capacities at low C tests. The capacity increasing was also observed in other metal oxide systems [27], and the possible reason to explain this is the valence-related capacity increase and the surface related capacity rise.

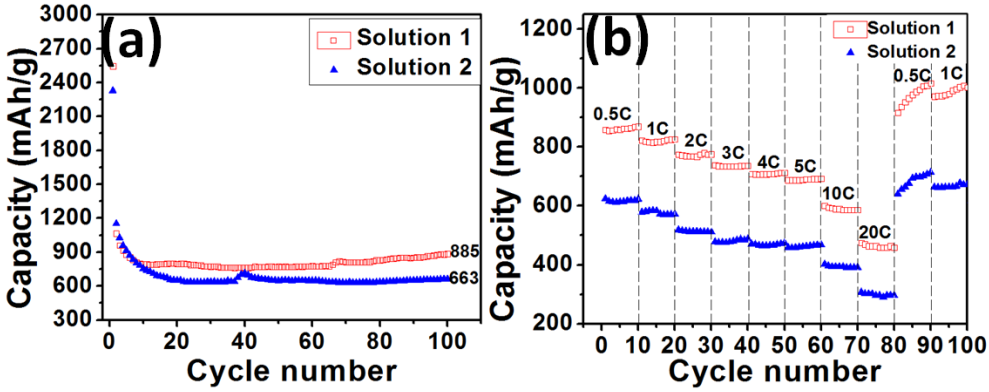

Figure 5. (a) Cyclability and (b) rate capability of the electrodes derived from solution 1 and solution 2.

3.3 Other applications of ESD

Besides fabricating electrodes for LIBs, ESD is widely applied in other areas due to its simplicity and good control for tailoring film compositions and morphologies. In this part, we will briefly review some of its applications. C-MEMS based 3D graphene nanosheets encrusted carbon micropillars by combining top-down (photo-lithography) and bottom-up processes (ESD) [28]. Graphene was successfully coated onto 3D carbon micropillars shown in Figure 6 (a). The graphene/carbon micropillar electrode arrays showed faster charge transfer and higher electrochemical activity towards H_2O_2 as compared to bare carbon micropillar electrode arrays. A linear response towards H_2O_2 was observed at a range of detection from 250µM to 5.5mM for graphene/carbon micropillar electrode. It is believed that the enhanced performance is a result of the unique structures created by ESD and that the method can be extended to conformally coat different functional nanomaterials onto high aspect ratio microstructures for wafer-level processing. For C-MEMS based micro-supercapacitor, in order to further improve the electrochemical performance, carbon nanotubes (CNTs)/C-MEMS composites were fabricated as electrode materials [29]. The iron catalyst particles that were later used to grow CNTs in

CVD process were first deposited on C-MEMS microstructures by ESD for 90 minutes. The resulting structures were shown in figure 6 (b) and (c). The specific capacitance of CNT/C-MEMS composites reached as high as 33F/g, which was 20 times higher compared to that of bare C-MEMS structure. Other than catalyst deposition, active materials can also be directly deposited on the desired structures. Figure 6 (d) shows the schematic drawing of fabrication procedures of micro-supercapacitors. Graphene oxide and CNTs were active materials and deposited on the designed structure through ESD [30]. The CNTs act as spacers for reduced graphene oxide and reduce the possibility of re-stacking which helps to maintain the high accessible surface area for electrolyte ions. Figure 6 (e) and (f) display the top and cross-section view of deposited rGO/CNTs composites. As the results indicate, a specific capacitance of 6.1 mF cm^{-2} was achieved at 0.01 V s^{-1} scan rate. An unprecedented specific capacitance of 2.8 mF cm^{-2} (stack capacitance of 3.1 F cm^{-3}) was recorded at a very high scan rate of 50 V s^{-1}. This design resulted in a high-frequency response of 290.76 Hz with resistive-capacitive (RC) time constants as low as 4.8 m s.

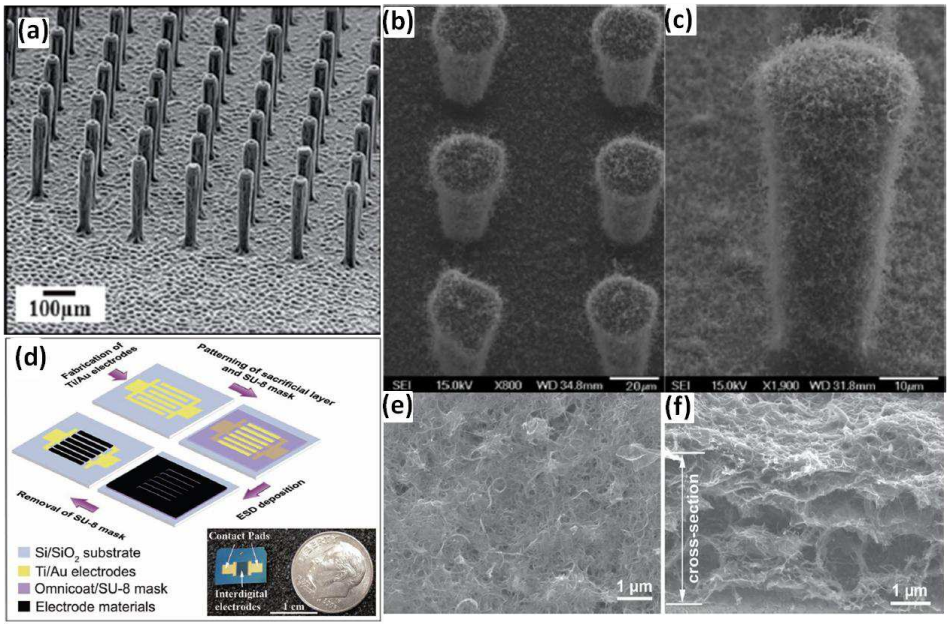

Figure 6. (a) Typical SEM images of graphene deposited carbon micropillars under conditions of 200 ^{0}C for 60 min; (b-c) SEM images of CNT/C-MEMS samples at a deposition time of 30 min; (d) Schematic drawing of fabrication procedures of micro-supercapacitors (inset shows a digital photograph of a fabricated device); (e-f) SEM images of the deposited electrodes rGO-CNT-8-2 microelectrodes.

4. Summary

The results from our research indicated that ESD has comprehensive superiority as compared to other traditional methods, especially for addressing some of the important issues of LIBs. It is also a useful technique that can be applied to the fields other than LIBs. We anticipate that further improvement in the performance of LIBs can be achieved and it deserves more extensive attention and development in the future.

Acknowledgments

This work was financially supported by the NSF NERC-Advanced Self-Powered Systems of Integrated Sensors and Technologies (ASSIST) center. R.A. acknowledges University Graduate School (UGS) at Florida International University for awarding Presidential Fellowship. The authors also would like to thank the staff members of Advanced Materials Engineering Research Institute (AMERI) facility at Florida International University for their kind help during experiments.

References

1. B. Dunn, H. Kamath and J. M. Tarascon, *Science*, **334**, 928 (2011).
2. A. Manthiram, A. V. Murugan, A. Sarkar, T. Muraliganth, *Energy Environ. Sci.*, **1**, 621 (2008).
3. H. G. Zhang, X. D. Yu, P. V. Braun, *Nat. Nanotechnol.*, **6**, 277 (2011).
4. M. F. El-Kady, V. Strong, S. Dubin, R. B. Kaner, *Science*, **335**, 1326 (2012) .
5. J. You, L. Dou, K. Yoshimura, T. Kato , K. Ohya, T. Moriarty , K. Emery, C. C. Chen, J. Gao, G. Li, Y. Yang, *Nat. Commun.*, **4** , 1446 (2013).
6. D. Fauteux and R. Koksbang, *J. Appl. Electrochem*., **23**, 1 (1993).
7. D. Aurbach and M.D. Levi, *J. Phys. Chem. B*., **101**, 4630 (1997).
8. D. Aurbach, E. Zinigrad, H. Teller and P. Dan, *J. Electrochem. Soc*., **147**, 1274 (2000).
9. C. K. Chan, X. F. Zhang, Y. Cui, *Nano Lett.*, **8** (1), 307 (2008).
10. X. F. Li, A. Dhanabalan and C. L. Wang, *Adv. Energy Mater*., **2**, 238 (2012).
11. Y. Yu, L. Gu, A. Dhanabalana, C. H. Chen and C. L. Wang, *Electrochim. Acta*, **54**, 7227 (2009).
12. X. F. Li, A. Dhanabalan K. Bechtold and C. L. Wang, *Electrochem. Commun*., **12**, 1222 (2010).
13. R. Dedryvere, S. Laruelle, S. Grugeon, P. Poizot, D. Gonbeau and T. M. Tarascon, *Chem. Mater.*, **16**, 1056 (2004).
14. S. Boyanov, D. Zitoun, M. Menetrier, J. C. Jumas, M. Womes and L. Monconduit, *J. Phys. Chem. C*, **113**, 21441 (2009).
15. N. Yamakawa, M. Jiang and C. P. Gery, *Chem. Mater.*, **21**, 3162 (2009).
16. P. G. Bruce, *Angew. Chem. Int. Ed*., **47**, 2930 (2008).
17. A. A. Zomeren, E. M. Kelder, J. C. M. Marijnissen and J. Schoonman, *J. Aerosol Sci.*, **25**, 1229 (1994).
18. C. M. Ghimbeu, J. Schoonman and M. Lumbreras, *Ceram. Int.*, **34**, 95 (2008).
19. C. H. Chen, E. M. Kelder, P. J. J. M. Van der Put and J. Schoonman, *J. Mater. Chem*., **6**,765 (1996).
20. X. Li, A. Dhanabalan, X. Meng, L. Gu, X. Sun and C. Wang, *Microporous Mesoporous Mater.*, **15**, 488 (2012).
21. X. Li and C. Wang, *J. Mater. Chem. A*, **1**, 165 (2013).
22. A. Dhanabalan, Y. Yu, X. Li, W. Chen, K. Bechtold, L. Gu and C. Wang, *J. Mater. Res.*, **25**, 8 (2010).
23. A. Dhanabalan , X. Li , R. Agrawal , C. Chen and C. Wang, *Nanomaterials*, **3**(4), 606 (2013).
24. P. Poizot, S. Laruelle, S. Grugeon, L. Dupont and J. M. Tarascon, *Nature*, **407**, 496 (2000).

25. Y. Yu, C. H. Chen, J. L. Shui and S. Xie, *Angew. Chem., Int. Ed.*, **44**, 7085 (2005).
26. B. Sun, J. Horvat, H. S. Kim, G. Wang, *J. Phys. Chem. C*, **114**, 18753 (2010).
27. Y. Yu, Y. Shi and C. H. Chen, *Nanotechnology*, **18**, 055706 (2007).
28. V. Penmatsa, T. Kim, M. Beidaghi, H. Kawarada, Z. Wang, L. Gu and C. Wang, *Nanoscale*, **4**, 3673(2012).
29. W. Chen, M. Beidaghi, V. Penmatsa, W. Li and C. Wang, *IEEE Nanotechm*, **9**, 1222 (2010).
30. M. Beidaghi, C. Wang, *Adv. Func. Mater.* **22**, 4501 (2012).